PAPER

Check for updates

Mixing mechanisms of lead nanoparticles with mineral particles: implication of atmospheric transportation of lead†

Yongpeng Ji,[ab] Qiuju Shi,[ab] Baocong Zhao,[ab] Ziqi Wu,[ab] Jiaxin Wang,[ab] Weina Zhang,[ab] Jiangyao Chen, [iD][ab] Yuemeng Ji [iD] *[ab] and Taicheng An [iD][ab]

Atmospheric mixing particles play a significant role in the ecosystem but is poorly quantified for the effect on climate and air quality, especially for the mixing of sand dust (mineral particles) and anthropogenic pollution (heavy metals) over East Asia. Hence, by combining molecular dynamics (MD) simulations and density functional theory (DFT) calculations, we investigated the mixing mechanisms of typical Pb nanoparticles (PbO, $PbSO_4$, $PbCO_3$, $PbCl_2$ and PbS) with sand and dust (SD) particles (Al_2O_3) in the atmosphere. Our MD simulations show that five target Pb nanoparticles get rapidly mixed with Al_2O_3 and are then retained on the surface, with three interfacial patterns of monodentate, bidentate and tridentate modes according to the interaction form of Pb atoms with Al_2O_3. Further DFT calculations reveal that the mixing ability of the oxygenated Pb nanoparticles with Al_2O_3 depends on the distances of Pb nanoparticles with the Al_2O_3 surface and the lengths of short hydrogen bonds; however, for non-oxygenated Pb nanoparticles, it is relevant to the length of long hydrogen bonds. Chemical bonding analyses show that after mixing, the interaction strength of Pb particles with Al_2O_3 follows the order of tridentate > bidentate > monodentate modes. The diffusion coefficients of mixed Pb nanoparticles are significantly lower than those of the unmixed Pb particles, resulting in stabilization, and the mixed oxygenated Pb nanoparticles are more stable than non-oxygenated Pb nanoparticles. Our results highlight the important role of SD particles in the capture and restriction of Pb nanoparticles and the necessity to account for the potential transport route of Pb nanoparticles with SD particles.

Environmental significance

Approximately 800 million tons of sands turn to airborne aerosols from Northern China, which is one of the major sources of sand and dust (SD) in East Asia. Atmospheric nanoparticle mixing state, such as SD particles mixing with heavy metal (Pb), plays a significant effect on air quality and human health. From combined molecular dynamics and density functional theory, we show the mixing mechanisms of Pb nanoparticles with Al_2O_3, including uptake processes, interfacial structures, and influences of interaction patterns on the mechanisms. Our work reveals that Pb nanoparticles are substantially restricted on Al_2O_3 and highlights the necessity to account for the potential transport route of Pb nanoparticles with SD particles.

1. Introduction

The major cities in Northern China have been frequently struck by sand and dust (SD) storms,[1–3] and especially the

[a] Guangdong-Hong Kong-Macao Joint Laboratory for Contaminants Exposure and Health, Guangdong Key Laboratory of Environmental Catalysis and Health Risk Control, Institute Environmental Health and Pollution Control, Guangdong University of Technology, Guangzhou 510006, China. E-mail: jiym@gdut.edu.cn
[b] Guangzhou Key Laboratory of Environmental Catalysis and Pollution Control, Key Laboratory for City Cluster Environmental Safety and Green Development of the Ministry of Education, School of Environmental Science and Engineering, Guangdong University of Technology, Guangzhou 510006, China

† Electronic supplementary information (ESI) available. See DOI: https://doi.org/10.1039/d3en00805c

most intense and widespread SD storm appeared on March 14–15, 2021 in the past decade. This SD storm event resulted in a significant enhancement in the maximum concentration of particulate matter with diameters <10 μm, reaching 3600 μg m^{-3} in Beijing.[1] Approximately 800 million tons of sand was turned into airborne aerosols from Northern China, which is one of the major sources of SD in East Asia.[1,4,5] The SD particles affected and altered the air quality by providing the reaction interfaces for anthropogenic pollutants,[6–17] human health was affected through the attack on the respiratory system,[18–20] and the climate and weather systems were impacted by changing the radiation balance.[21–24] More importantly, the SD particles mixed with the anthropogenic

pollutants,[22,25–30] such as heavy metals, organic and inorganic compounds, and biomaterials were transported to the areas without SD storms,[31,32] leading to a wide-ranging risk to the environment.

Atmospheric heavy metals are important anthropogenic pollutants, which are unequivocally associated with increased cardiovascular and respiratory diseases and increased risk of cancer.[33–36] Lead (Pb), as a highly toxic heavy metal, is emitted into the atmosphere from coal combustion, industrial activities, waste incineration, non-ferrous metal mining, and smelting.[29,37–40] Some previous field studies have revealed that SD particles are mixed with the anthropogenic Pb to form atmospheric particle-bound Pb along the transport pathways of SD storms, leading to a high concentration of Pb during the SD storm period.[41–48] Atmospheric particle-bound Pb is inhaled into and accumulated in the human body, causing potential adverse effects on human health.[49,50] They also act as cloud condensation nuclei and ice condensation nuclei to affect the global radiation balance.[27,28,51] Hence, besides the estimation of the amount of particle-bound Pb ingested, it is also essential to systematically study the formation mechanism of atmospheric particle-bound Pb and its impact on the environment.

In the atmosphere, field measurements have observed five main particle forms of element Pb, including lead oxides (PbO), sulfates ($PbSO_4$), carbonates ($PbCO_3$), chloride ($PbCl_2$), and sulfides (PbS), which are mainly discharged into the environment from mining activity, coal combustion, and smelting.[52–57] Falgayrac et al. found that the heterogeneous reactions of $PbSO_4$ on calcite surfaces produced $Pb_3(CO_3)_2(OH)_2$ and $PbCO_3$ on calcite surfaces using Raman microimaging.[58,59] At low relative humidity (RH), there is only external mixing of $PbSO_4$ and $CaCO_3$ rather than any internal mixing. However, Ishizaka et al.[60] have shown that different products from the reactions of $PbSO_4$ on calcite surfaces were obtained after the long reaction time using X-ray absorption. Hence, the heterogeneous formation mechanisms of particle-bound Pb from SD particles with five main Pb particle forms remain unclear.

Hence, the mixing mechanisms of the five Pb nanoparticles with SD particles were investigated using theoretical approaches. Herein, γ-Al_2O_3(110), as a reactive crystalline form of alumina (Al_2O_3) with high surface area,[61–64] was chosen as the model of Al_2O_3 because Al_2O_3 is a type of major SD particle in the atmosphere.[65] The uptake process of each Pb nanoparticle with Al_2O_3 was simulated by molecular dynamics (MD) simulation, and the patterns of the SD-bound Pb nanoparticles were identified. The patterns for the SD-bound Pb nanoparticles were then constructed using the density functional theory (DFT), and their chemical properties were analyzed. Combining the two approaches mentioned above, the mixing mechanisms of five Pb nanoparticles with Al_2O_3 were established. Diffusion coefficients of five Pb nanoparticles were calculated to reveal the mobility of five Pb nanoparticles with and without Al_2O_3 and to evaluate the implications of the transport for Pb nanoparticles.

2. Methods

2.1 Molecular dynamics simulations

All classical MD simulations were performed using the large-scale atomic/molecular massively parallel simulator (LAMMPS) simulation package.[66] A (25 × 25) γ-Al_2O_3 (110) model with eight layers of atoms was constructed, and for convenience, this model was denoted as Al_2O_3. To simulate the real surface state of γ-Al_2O_3 (110) under ambient atmospheric conditions, the top and bottom of the Al_2O_3 surface were hydroxylated in periodic simulations. Five target Pb nanoparticles, including PbS, $PbCl_2$, PbO, $PbCO_3$, and $PbSO_4$ nanoparticles, were constructed with 16 molecules for each Pb nanoparticle, and the volume of all Pb nanoparticles are almost 1 nm^3. The total size of the simulation box in each mixing system was approximately 214 × 205 × 210 $Å^3$. As discussed in the ESI,† for each mixing system, four Pb nanoparticles were placed into the simulation box along with N_2 and O_2 molecules. A 3.0 ns MD simulation with a time step of 1.0 fs was carried out in each mixing system in the isothermal–isobaric (NPT) ensemble for equilibration (P = 1 atm, T = 298.15 K). Al_2O_3 was described from the ClayFF force field,[67] N_2 and O_2 were described by the INTERFACE force field (IFF) interaction potentials,[68] and the five target Pb nanoparticles were performed by the force field parameters calculated using the Sobtop program[69] and Seminario method.[70] The partial charges of the atoms involved in the five Pb nanoparticles were employed with a density-derived electrostatic and chemical (DDEC)[71,72] charge scheme. The periodic boundary conditions were applied along the X, Y and Z directions and a cut-off distance of 12.0 Å was smoothly truncated for the short-range interactions. The long-range electrostatic interactions were computed using the particle–particle–particle-mesh (PPPM) summation algorithm with an accuracy of 10^{-5}.[73] The MD trajectories were visualized using the OVITO software,[74] and the analyses of the atomic density profiles (ADPs) were performed via VMD[75,76] using the trajectories of the last 1 ns in the whole simulation time of 3 ns. ADPs were calculated according to the following equation:

$$\rho(z) = \frac{N(\Delta z)}{V}$$

where $\rho(z)$ represents ADPs, $N(\Delta z)$ is the average number of atoms in a small bin of thickness Δz in the z-axis of the simulation box and V denotes the volume of the simulation box.

2.2 Density functional theory calculations

All DFT calculations were performed using the plane-wave level utilizing the Vienna ab initio simulation package (VASP).[77] The Perdew–Burke–Ernzerhof (PBE)[78] and the generalized gradient approximation (GGA) exchange-correlation functional were carried out to investigate the electron interactions. The core electrons were described with the projector augmented wave (PAW) method.[79] The cutoff

energy was set to 400 eV, and the convergence criterion of the structural optimization was −0.01 eV Å^{-1}. A (1 × 1) hydroxylated γ-Al$_2$O$_3$ (110) surface with four layers was constructed. The vacuum region was set to approximately 15 Å to eliminate the interactions between each slab. A 3 × 3 × 1 Monkhorst–Pack k-point grid was applied. The dispersion corrections were considered using the DFT-D3(BJ) scheme.[80,81] Crystal orbital Hamilton population (COHP) was used to analyze the chemical bonding using the LOBSTER program.[82,83] The band structures and density of states (DOS) were calculated using the hybrid HSE06 functional.[84] All atoms were allowed to relax in all calculations. In this work, the mixing energy (ΔE) was defined as Δ$E = E_{(Al_2O_3–Pb)} − (E_{Al_2O_3} + E_{Pb})$, where $E_{(Al_2O_3–Pb)}$ represents the energy of the heterocomplex, and $E_{Al_2O_3}$ and E_{Pb} are the energies of Al$_2$O$_3$ and Pb, respectively.

3. Results and discussion

3.1 Uptake of Pb nanoparticles onto Al$_2$O$_3$

To systematically understand the behavior of Pb nanoparticles mixed with Al$_2$O$_3$, the uptake process, as the first step in the mixing process, was simulated using MD simulations (Fig. S1†). To describe the equilibrium trajectories of the uptake and mixing process, some typical snapshots of five Pb nanoparticles (i.e., PbS, PbCl$_2$, PbO,

PbCO$_3$, and PbSO$_4$) mixed with Al$_2$O$_3$ were selected and are presented in Fig. 1 and S2.† All Pb nanoparticles were retained by the hydroxyl surface of Al$_2$O$_3$ during the simulation time. Especially, for non-oxygenated Pb nanoparticles (PbS and PbCl$_2$), there is an intermolecular mobility from the top-layer atoms of the non-oxygenated Pb nanoparticles to the Al$_2$O$_3$ surface (Fig. S2†), leading to a structural reconstruction of the non-oxygenated Pb nanoparticles after the uptake onto the Al$_2$O$_3$ surface. It is evident from Fig. 1 and S2† that the atomic percentages of non-oxygenated Pb nanoparticles exhibiting direct coordination with Al$_2$O$_3$ surface are 57.8% and 80.5% for PbCl$_2$ and PbS nanoparticle systems, respectively, higher than those of oxygenated Pb nanoparticles.

To explore the interfacial patterns between Pb nanoparticles with the Al$_2$O$_3$ surface, the typical configurations from the mixing trajectories are presented in Fig. 2 and S3.† Pb nanoparticles coordinate to the Al$_2$O$_3$ surface in three different modes depending on the type of interaction between the Pb atom and O atom (O$_{Al}$) of the Al$_2$O$_3$ surface, i.e., monodentate (MDT), bidentate (BDT), and tridentate (TDT) modes. The branching ratio of the three modes was estimated, as shown in Fig. 2 and S3.† For the oxygenated Pb nanoparticle systems, there existed the MDT, BDT, and TDT modes but the TDT mode was only observed in PbCO$_3$ and PbSO$_4$ nanoparticle systems. The interfacial
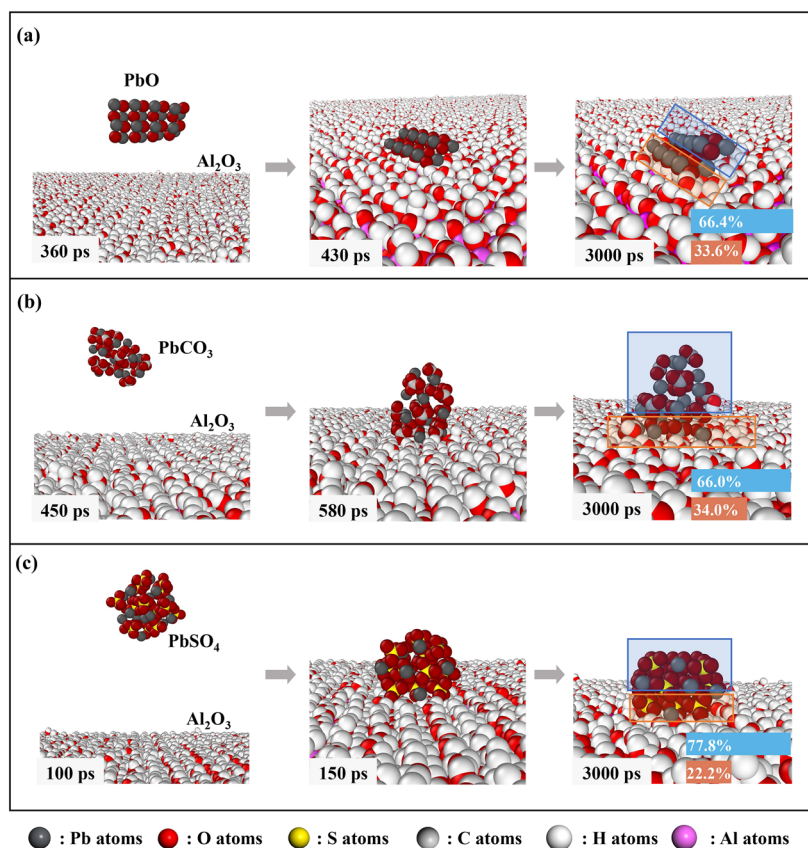

Fig. 1 Selected snapshots of the MD trajectories for (a) PbO, (b) PbCO$_3$ and (c) PbSO$_4$ nanoparticle systems. Percentages are atoms in Pb nanoparticles that directly (orange area) and indirectly (blue area) coordinate with Al$_2$O$_3$.
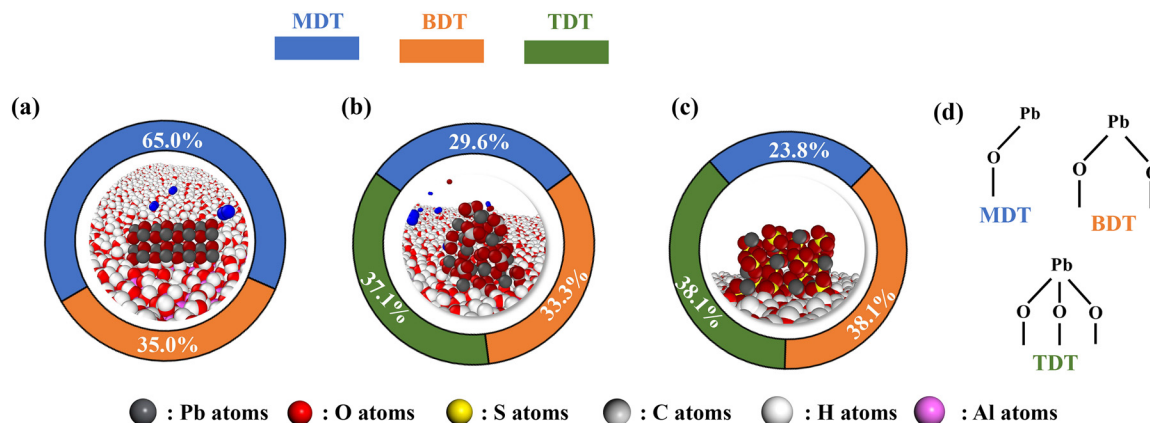
Fig. 2 The branching ratios of the interfacial patterns between Pb nanoparticles with Al_2O_3 in (a) PbO, (b) $PbCO_3$ and (c) $PbSO_4$ nanoparticle systems and (d) diagram for three interfacial patterns of MDT, BDT, and TDT.

pattern is dominated by the MDT mode in PbO nanoparticle systems with 65.0%, by the TDT mode in $PbCO_3$ nanoparticle systems with 37.1%, and by BDT and TDT modes in $PbSO_4$ nanoparticle systems with both being 38.1%. However, there are no TDT modes in the non-oxygenated Pb nanoparticle systems. For non-oxygenated Pb nanoparticle systems, the large branching ratios are MDT modes in the PbS nanoparticle system with 51.1% and the BDT mode in the $PbCl_2$ nanoparticle system with 71.4%.

The atomic density profiles (ADPs) of Pb nanoparticles as functions of the distance normal onto the surface of Al_2O_3 are displayed in Fig. 3 and S4.† For the oxygenated Pb nanoparticle systems, the interaction of PbO nanoparticles with the Al_2O_3 surface is predominantly driven by the O_{PbO} atom and is characterized by the first peak at ~1.7 Å. However, the Pb atom is primarily located at the larger distance, which is evident from the presence of the first peak at ~2.4 Å from the Al_2O_3 surface (Fig. 3a). Similar results can be drawn from other oxygenated Pb nanoparticle systems

($PbCO_3$ and $PbSO_4$). Such distributions suggest that the interactions between the O atom and the Al_2O_3 surface are stronger than those of the Pb atom with Al_2O_3. However, for non-oxygenated Pb nanoparticle systems, the ADPs clearly illustrate that there exist negligibly differences in the interfacial interaction of all atoms of Pb nanoparticles with the Al_2O_3 surface. For example, the first peaks of Pb and S atoms in the PbS nanoparticles system are both located at ~1.9 Å. Furthermore, the ADPs of the oxygenated Pb nanoparticles exhibit the first peaks at distances of approximately 1.5 Å, which are smaller than those of the non-oxygenated Pb nanoparticles. It indicates that the oxygenated Pb nanoparticles are more easily mixed with Al_2O_3 than the non-oxygenated Pb nanoparticles.

3.2 Mixing mechanisms of Pb nanoparticles with Al_2O_3

Due to the limitation of chemical bonds and the charge transfer in the classical molecular dynamic model, to provide insight into the interaction of Pb nanoparticles with the Al_2O_3 surface and the nature of the mixing mechanisms, we performed DFT calculations to investigate three distinct modes obtained through the MD simulations mentioned above in each of the Pb nanoparticle systems. Fig. 4 and S5† list the potential energy surfaces (PESs) of the three kinds of modes in the oxygenated and non-oxygenated Pb nanoparticle systems, respectively, along with the corresponding optimized geometries. Depending on the lengths of the hydrogen bonds, two types of hydrogen bonds were found and studied, i.e. short hydrogen bonds (SHBs) and long hydrogen bonds (LHBs) between the non-metallic atoms (O, Cl and S atoms) of Pb nanoparticles and H atoms of Al_2O_3.

For the PbO nanoparticle system, only BDT heterocomplexes are formed, but no MDT heterocomplex was obtained, such that even a favorable initial configuration was provided for forming MDT. The different results, compared with MD simulations, are explained by interfacial adsorption structures because covalent bonds are formed. As shown in
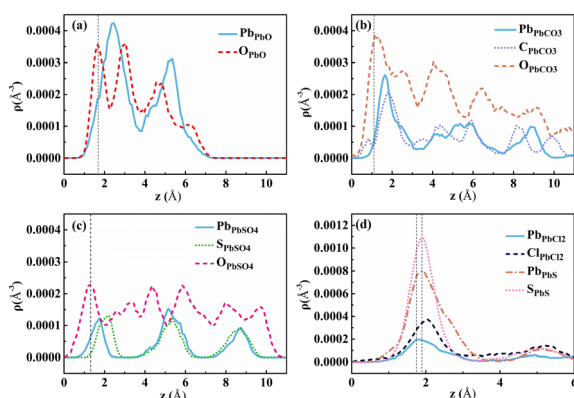

Fig. 3 Atomic density profiles (ADPs) of Pb nanoparticles as functions of distance from Al_2O_3 surface for (a) PbO, (b) $PbCO_3$, (c) $PbSO_4$, (d) $PbCl_2$ and PbS nanoparticle systems. The mean positions for the H atoms of upper Al_2O_3 surface are z = 0 Å. The locations of the ADPs peaks represent the average distance between the corresponding atoms with the Al_2O_3 surface.
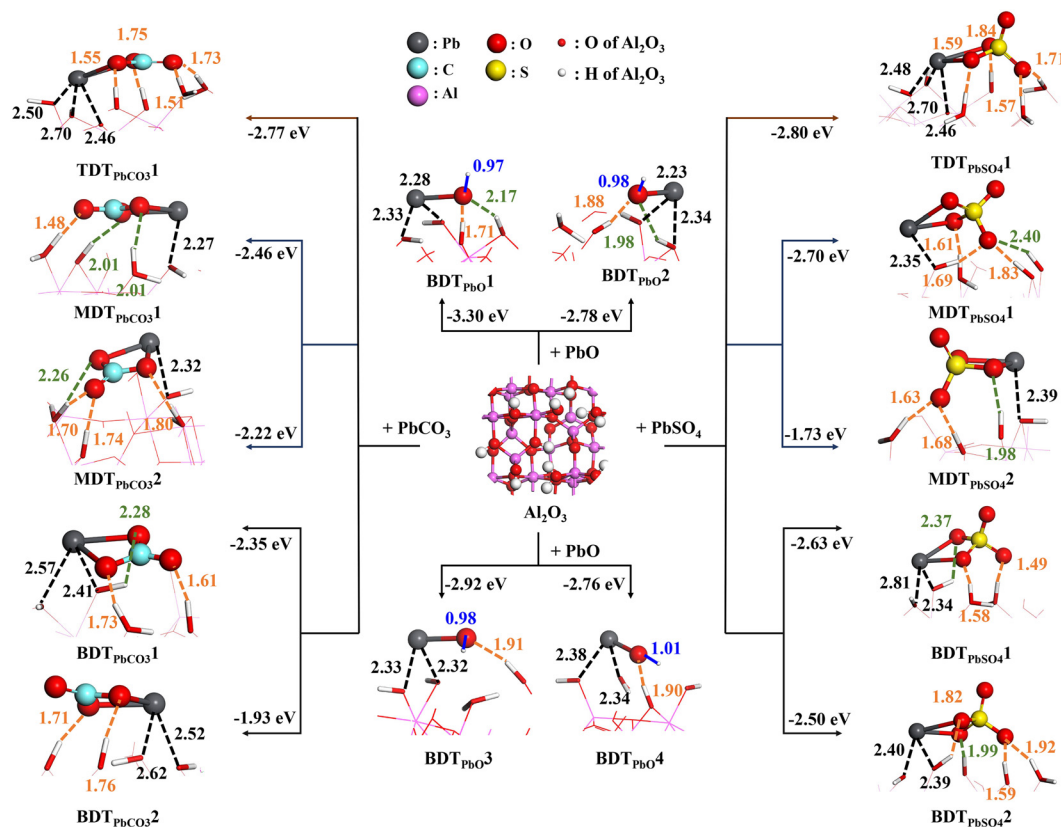
Fig. 4 Potential energy surfaces of the mixing pathways in oxygenated Pb nanoparticle systems, along with the optimized geometries. The numbers in eV denote the mixing energies, and other numbers represent bond lengths in Å.

Fig. 4, the H atom of Al_2O_3 (H_{Al}) is completely pulled out from Al_2O_3 surface by the O atom of PbO (O_{PbO}) in four BDT heterocomplexes, suggesting the formation of the O_{PbO}–H_{Al} covalent bonds with the distance from 0.97 to 1.01 Å (Fig. 4). For four BDT heterocomplexes, except for the two Pb–O_{Al} bonds, there are two distinct hydrogen bonds between O_{PbO} and H_{Al}, *i.e.* SHBs and LHBs. $BDT_{PbO}1$ possesses the largest negative ΔE value of −3.30 eV among the four heterocomplexes, corresponding to the shortest SHB, and O_{PbO}–H_{Al} covalent bond. For the other two oxygenated Pb nanoparticle systems, the lowest ΔE values appear at the TDT mode with −2.77 eV for the $PbCO_3$ nanoparticle system and −2.80 eV for the $PbSO_4$ nanoparticle system. Most numbers of SHBs exist in $TDT_{PbCO_3}1$ and $TDT_{PbSO_4}1$ among all heterocomplexes in TDT modes. In addition, no extra covalent bond was formed for $PbCO_3$ and $PbSO_4$ nanoparticle systems. Hence, the stability of the heterocomplex in the mixing process of PbO with Al_2O_3 is relevant to the distance of the nanoparticle with the surface; however, in the absence of the extra covalent bond, the stability of the heterocomplex is regulated by the numbers and lengths of SHBs for $PbCO_3$ and $PbSO_4$ nanoparticle systems.

For the non-oxygenated Pb nanoparticle systems, there is no formation of TDT heterocomplexes. As shown in Fig. S5,† two heterocomplexes are formed in BDT and MDT modes for the $PbCl_2$ nanoparticle system, but there are three

heterocomplexes in the BDT mode and one in the MDT mode for the PbS nanoparticle system. In all heterocomplexes, no SHBs were found for non-oxygenated Pb nanoparticle systems. The BDT and MDT heterocomplexes with the shortest LHBs correspond to the most negative ΔE values for $PbCl_2$ and PbS nanoparticle systems. For example, for the $PbCl_2$ nanoparticle system, the distances of LHBs in $BDT_{PbCl_2}1$ are 2.04 and 2.09 Å, which are shorter than those in other BDT heterocomplexes, and the corresponding ΔE value of −2.00 eV is smaller than those of other BDT heterocomplexes. It indicated that for the non-oxygenated Pb nanoparticle systems, all BDT and MDT heterocomplexes include Pb–O_{Al} bonds and LHBs, and their stabilities depend on the lengths of LHBs.

3.3 Analysis of DOS and COHP

To interpret the chemical bonding of Pb nanoparticles upon the mixing process, the valance band maximum (VBM) and the conduction band minimum (CBM) of the Pb molecule before and after mixing were analyzed by DOS (Fig. S6†). The VBM of the Pb molecule mainly consists of non-metallic atoms (O, Cl and S atoms), while the CBM is composed of metallic atoms (Pb atoms). After mixing, the energies in PbO and $PbCO_3$ nanoparticle systems decreased for the VBM but they increased for CBM, and the energies

of VBM and CBM increased in $PbSO_4$, $PbCl_2$ and PbS nanoparticle systems because of a significant delocalization of the electron density. It indicates that the orbital energies of the Pb molecule are altered by the bonding of the Pb molecule with Al_2O_3, forming the stable heterocomplex in each system. The detailed chemical bonding ($Pb–O_{Al}$) is revealed by COHP analysis and listed in Fig. S7.† The bonding area (positive peaks) below the Fermi level includes three regimes, that is, the interaction between $Pb(6p)$ and $O_{Al}(2s)$, between $Pb(6p)$ and $O_{Al}(2p)$, and between $Pb(6s)$ and $O_{Al}(2p)$, suggesting that the major contribution of the $Pb–O_{Al}$ bonds is due to electron sharing between the $Pb(6p/6s)$ and $O_{Al}(2p/2s)$ orbitals.

Integrated crystal orbital Hamilton population (ICOHP) is an effective approach to evaluate the bonding strength. The more negative the ICOHP value has, the stronger the bonding strength is. The ICOHP of each $Pb–O_{Al}$ bond in heterocomplexes and the total ICOHP value (*i.e.* TICOHP, the sum for the ICOHP values of all $Pb–O_{Al}$ bonds in each heterocomplex) are listed in Table S1.† The TICOHP value of each TDT heterocomplex is lower than that of MDT and BDT heterocomplexes. For example, for the $PbCO_3$ nanoparticle system, the TICOHP value of $TDT_{PbCO_3}1$ is −4.20 eV, 0.89 and 1.32 eV lower than those of $BDT_{PbCO_3}1$ and $MDT_{PbCO_3}1$, respectively. In addition, the TICOHP value of each BDT heterocomplex is smaller than that of the MDT heterocomplex. For example, the TICOHP value of $BDT_{PbCl_2}1$ is −3.15 eV, which is 0.57 eV smaller than that of $MDT_{PbCl_2}1$. It suggests that there is a stronger interaction between the Pb nanoparticle and Al_2O_3 in the BDT heterocomplex than in the MDT heterocomplex. However, in $PbCO_3$ and $PbSO_4$ nanoparticle systems, the MDT heterocomplexes are thermodynamically more favorable to be formed than the BDT heterocomplexes, attributable to the formation of strong hydrogen bonds in MDT heterocomplexes.

3.4 Mobility of Pb nanoparticles on Al_2O_3 surface

To estimate the mobility of Pb nanoparticles on the Al_2O_3 surface, the diffusion coefficients (DC_{mix}s) of the five Pb nanoparticles on the Al_2O_3 surface at 298.15 K were calculated using the mean square displacements (Table S2†). For oxygenated Pb nanoparticle systems, the DC_{mix}s of PbO, $PbCO_3$ and $PbSO_4$ nanoparticles are 1.25×10^{-10}, 1.59×10^{-10} and 1.85×10^{-10} m^2 s^{-1}, respectively, with the order of DC_{mix} (PbO) $< DC_{mix}$ ($PbCO_3$) $< DC_{mix}$ ($PbSO_4$). That is, the mobility is enhanced from PbO to $PbCO_3$ to $PbSO_4$ nanoparticles after mixing with Al_2O_3. The small mobility of the PbO nanoparticles corresponds to the low mixing energy, indicating that the mobility of the oxygenated Pb nanoparticles is related to the interaction strength between Pb nanoparticles and Al_2O_3. However, for the non-oxygenated Pb nanoparticle systems, the large DC_{mix} of Pb nanoparticles corresponds to the low mixing energy. For example, the $PbCl_2$ nanoparticle possesses a large DC_{mix} with 2.40×10^{-9} m^2 s^{-1} but a low mixing energy with −2.00−−1.85 eV. It suggests that

for the non-oxygenated Pb nanoparticle systems, although there exists a strong interaction between $PbCl_2$ nanoparticles and Al_2O_3, $PbCl_2$ nanoparticles more easily escape from Al_2O_3 than PbS nanoparticles after mixing with Al_2O_3.

On the other hand, the DC_{mix}s of PbS and $PbCl_2$ nanoparticles are at least nine times higher than those of the three oxygenated Pb nanoparticles, indicating that oxygenated Pb nanoparticles are readily restricted onto the Al_2O_3 surface. It indicates that the mobility restriction of the oxygenated Pb nanoparticles by Al_2O_3 is stronger than that of the non-oxygenated Pb nanoparticles. For comparison, the DC_{air}s of five Pb nanoparticles without Al_2O_3 were also computed and are listed in Table S2.† The DC_{mix}s of the Pb nanoparticles vary from 1.25×10^{-10} to 2.40×10^{-9} m^2 s^{-1}, which are lower by 2–3 orders of magnitude than those of the unmixed Pb nanoparticles. Hence, there is a significant restriction of Pb nanoparticles when they are mixed with Al_2O_3.

4. Conclusions and environmental implications

Sand and dust (SD) particles transport with SD storms starting from the Mongolian, Taklimakan, and Gobi Deserts, and significantly affect Northern China.[85,86] During long-distance transport, they combine with anthropogenic pollutants[22,25–29] and form mixing particles, with implications for climate, air quality, and human health.[18,19,21–23] Atmospheric particle-bound Pb, formed by the mixing of Pb nanoparticles with SD particles in the SD storm period,[41–48] can be inhaled into the human body and cause serious health hazards.[49,50] Hence, we investigated the mixing mechanisms of several typical Pb nanoparticles (such as PbO, $PbSO_4$, $PbCO_3$, $PbCl_2$ and PbS) with SD particles (such as Al_2O_3) by MD simulations and DFT calculations. Our MD simulation results reveal that five Pb nanoparticles are retained on the surface with three interfacial patterns of MDT, BDT and TDT modes. The mixing pathways of the three patterns obtained in DFT calculations provided insights into the interaction of Pb nanoparticles with Al_2O_3. Except for $Pb–O_{Al}$ bonds, three types of extra bonds of covalent bonds, SHBs and LHBs are identified and our results reveal that the stability of heterocomplex is affected by the distance between Pb nanoparticles and Al_2O_3 and the lengths of SHBs and LHBs. Moreover, DOS and COHP analyses show that the stability for the three interfacial patterns follows the order of TDT > BDT > MDT modes.

On the other hand, Northwest China (upwind area) and North and East China (downwind area), as the representative areas along the transport pathway of the SD storm, were selected to assess the influence of the SD storm on the transport of Pb nanoparticles in Northern China. For Northwest China, there exist plenty of large mining sites[87,88] with abundant products containing PbS nanoparticles during mining and smelting activities.[53,54] Our calculated DC_{mix} of PbS nanoparticles is three orders of magnitude lower than that of DC_{air} (Table S2†), indicating that the mobility of PbS

nanoparticles is restricted by SD particles after mixing. Therefore, PbS nanoparticles from Northwest China can be transported with SD particles to the downwind area during the SD storm period with profound implications for air quality and human health. However, for North and East China, with large amounts of coal-fired power plants except for the mining sites and smelters, abundant oxygenated Pb nanoparticles will be produced *via* coal combustion.[52] The *DC*s results show that the restriction of oxygenated Pb nanoparticles by SD particles is stronger than that of the non-oxygenated Pb nanoparticles. Hence, in the presence of the SD particles, Pb nanoparticles from North and East China may affect wilder areas than those from Northwest China. Our MD and DFT results reveal the important contribution of SD particles on the capture and restriction of Pb nanoparticles and highlight the significant potential of oxygenated Pb nanoparticles to transport with the SD particles. Hence, additional studies should pay attention to the role of SD particles in the atmospheric transportation of Pb nanoparticles and the subsequent impact on ecosystems and human health. Source appointments of anthropogenic Pb are required in future studies to understand the contribution of emitted Pb from different communities to heavy metal pollution.

Author contributions

Yongpeng Ji: investigation, formal analysis, methodology, writing – original draft, data curation; Qiuju Shi, Baocong Zhao, ZiqiWu, Jiaxin Wang: investigation, methodology, formal analysis; Weina Zhang, Jiangyao Chen: visualization, writing – review and editing; Yuemeng Ji: conceptualization, funding acquisition, writing – original draft, writing – review and editing; Taicheng An: supervision, validation.

Conflicts of interest

The authors declare that they have no known competing financial interests or personal relationships that could have appeared to influence the work reported in this paper.

Acknowledgements

References

1 G. Li, D. Lu, X. Yang, H. Zhang, Y. Guo, G. Qu, P. Wang, L. Chen, T. Ruan, X. Hou, X. Jin, R. Zhang, Q. Tan, S. Zhai, Y. Ma, R. Yang, J. Fu, J. Shi, G. Liu, Q. Wang, Y. Liang, Q. Zhang, Q. Liu and G. Jiang, Resurgence of Sandstorms Complicates China's Air Pollution Situation, *Environ. Sci. Technol.*, 2021, **55**, 11467–11469.

2 C. Wu, S. Zhang, G. Wang, S. Lv, D. Li, L. Liu, J. Li, S. Liu, W. Du, J. Meng, L. Qiao, M. Zhou, C. Huang and H. Wang, Efficient Heterogeneous Formation of Ammonium Nitrate on the Saline Mineral Particle Surface in the Atmosphere of East Asia during Dust Storm Periods, *Environ. Sci. Technol.*, 2020, **54**, 15622–15630.

3 S. Chen, D. Zhao, J. Huang, J. He, Y. Chen, J. Chen, H. Bi, G. Lou, S. Du, Y. Zhang and F. Yang, Mongolia Contributed More than 42% of the Dust Concentrations in Northern China in March and April 2023, *Adv. Atmos. Sci.*, 2023, **40**, 1549–1557.

4 J. M. Creamean, K. J. Suski, D. Rosenfeld, A. Cazorla, P. J. DeMott, R. C. Sullivan, A. B. White, F. M. Ralph, P. Minnis, J. M. Comstock, J. M. Tomlinson and K. A. Prather, Dust and Biological Aerosols from the Sahara and Asia Influence Precipitation in the Western U.S, *Science*, 2013, **339**, 1572–1578.

5 T. D. Jickells, Z. S. An, K. K. Andersen, A. R. Baker, G. Bergametti, N. Brooks, J. J. Cao, P. W. Boyd, R. A. Duce, K. A. Hunter, H. Kawahata, N. Kubilay, J. laRoche, P. S. Liss, N. Mahowald, J. M. Prospero, A. J. Ridgwell, I. Tegen and R. Torres, Global Iron Connections Between Desert Dust, Ocean Biogeochemistry, and Climate, *Science*, 2005, **308**, 67–71.

6 C. E. Kolb, R. A. Cox, J. P. D. Abbatt, M. Ammann, E. J. Davis, D. J. Donaldson, B. C. Garrett, C. George, P. T. Griffiths, D. R. Hanson, M. Kulmala, G. McFiggans, U. Poeschl, I. Riipinen, M. J. Rossi, Y. Rudich, P. E. Wagner, P. M. Winkler, D. R. Worsnop and C. D. O'Dowd, An overview of current issues in the uptake of atmospheric trace gases by aerosols and clouds, *Atmos. Chem. Phys.*, 2010, **10**, 10561–10605.

7 X. He, Z. Ma, X. Xi, A. Kudesi and J. Wang, Heterogeneous reaction of toluene/NO_2/O_3 on α-Fe_2O_3 nanoparticles: the impacts of O_3, light illumination, and relative humidity on the formation of N-containing organic compounds (NOC), *Environ. Sci.: Nano*, 2022, **9**, 3318–3330.

8 Q. Ma, Y. Zhao, P. Zhang, C. Liu, T. Lin, L. Wang, B. Chu and H. He, Comprehensive study about the heterogeneous conversion of NH_3 on nanoscale TiO_2 particles: insight into the mechanism and atmospheric implications, *Environ. Sci.: Nano*, 2023, **10**, 241–250.

9 K. Li, L. Kong, A. Zhanzakova, S. Tong, J. Shen, T. Wang, L. Chen, Q. Li, H. Fu and L. Zhang, Heterogeneous conversion of SO_2 on nano α-Fe_2O_3: the effects of morphology, light illumination and relative humidity, *Environ. Sci.: Nano*, 2019, **6**, 1838–1851.

10 Y. Chen, S. Tong, W. Li, Y. Liu, F. Tan, M. Ge, X. Xie and J. Sun, Photocatalytic Oxidation of SO_2 by TiO_2: Aerosol Formation and the Key Role of Gaseous Reactive Oxygen Species, *Environ. Sci. Technol.*, 2021, **55**, 9784–9793.

11 Y. Chen, S. Tong, J. Wang, C. Peng, M. Ge, X. Xie and J. Sun, Effect of Titanium Dioxide on Secondary Organic Aerosol Formation, *Environ. Sci. Technol.*, 2018, **52**, 11612–11620.

12 M. Tang, X. Huang, K. Lu, M. Ge, Y. Li, P. Cheng, T. Zhu, A. Ding, Y. Zhang, S. Gligorovski, W. Song, X. Ding, X. Bi and X. Wang, Heterogeneous reactions of mineral dust aerosol: implications for tropospheric oxidation capacity, *Atmos. Chem. Phys.*, 2017, **17**, 11727–11777.

13 N. Yang, N. T. Tsona, S. Cheng, S. Li, L. Xu, Y. Wang, L. Wu and L. Du, Competitive reactions of SO₂ and acetic acid on alpha-Al₂O₃ and CaCO₃ particles, *Sci. Total Environ.*, 2020, **699**, 134362.

14 N. Yang, N. T. Tsona, S. Cheng, Y. Wang, L. Wu, M. Ge and L. Du, Effects of NO₂ and SO₂ on the heterogeneous reaction of acetic acid on alpha-Al₂O₃ in the presence and absence of simulated irradiation, *Environ. Sci.: Processes Impacts*, 2020, **22**, 408–417.

15 H. Wang, C. Peng, X. Wang, S. Lou, K. Lu, G. Gan, X. Jia, X. Chen, J. Chen, H. Wang, S. Fan, X. Wang and M. Tang, N₂O₅ uptake onto saline mineral dust: a potential missing source of tropospheric ClNO₂ in inland China, *Atmos. Chem. Phys.*, 2022, **22**, 1845–1859.

16 S. A. Styler and D. J. Donaldson, Heterogeneous Photochemistry of Oxalic Acid on Mauritanian Sand and Icelandic Volcanic Ash, *Environ. Sci. Technol.*, 2012, **46**, 8756–8763.

17 Y. Ji, X. Chen, Y. Xiao, Y. Ji, W. Zhang, J. Wang, J. Chen, G. Li and T. An, Assessing the role of mineral particles in the atmospheric photooxidation of typical carbonyl compound, *J. Environ. Sci.*, 2021, **105**, 56–63.

18 A. S. Goudie, Desert dust and human health disorders, *Environ. Int.*, 2014, **63**, 101–113.

19 A. Rashki, N. J. Middleton and A. S. Goudie, Dust storms in Iran - Distribution, causes, frequencies and impacts, *Aeolian Res.*, 2021, **48**, 100655.

20 H. Chen, Y. Lin, Q. Su and L. Cheng, Spatial variation of multiple air pollutants and their potential contributions to all-cause, respiratory, and cardiovascular mortality across China in 2015–2016, *Atmos. Environ.*, 2017, **168**, 23–35.

21 P. J. DeMott, A. J. Prenni, G. R. McMeeking, R. C. Sullivan, M. D. Petters, Y. Tobo, M. Niemand, O. Moehler, J. R. Snider, Z. Wang and S. M. Kreidenweis, Integrating laboratory and field data to quantify the immersion freezing ice nucleation activity of mineral dust particles, *Atmos. Chem. Phys.*, 2015, **15**, 393–409.

22 J. Huang, T. Wang, W. Wang, Z. Li and H. Yan, Climate effects of dust aerosols over East Asian arid and semiarid regions, *J. Geophys. Res.: Atmos.*, 2014, **119**, 11398–11416.

23 M. Tang, H. Zhang, W. Gu, J. Gao, X. Jian, G. Shi, B. Zhu, L. Xie, L. Guo, X. Gao, Z. Wang, G. Zhang and X. Wang, Hygroscopic Properties of Saline Mineral Dust From Different Regions in China: Geographical Variations, Compositional Dependence, and Atmospheric Implications, *J. Geophys. Res.: Atmos.*, 2019, **124**, 10844–10857.

24 P. Tian, X. Cao, L. Zhang, N. Sun, L. Sun, T. Logan, J. Shi, Y. Wang, Y. Ji, Y. Lin, Z. Huang, T. Zhou, Y. Shi and R. Zhang, Aerosol vertical distribution and optical properties over China from long-term satellite and ground-based remote sensing, *Atmos. Chem. Phys.*, 2017, **17**, 2509–2523.

25 P. Tian, L. Zhang, J. Ma, K. Tang, L. Xu, Y. Wang, X. Cao, J. Liang, Y. Ji, J. H. Jiang, Y. L. Yung and R. Zhang, Radiative absorption enhancement of dust mixed with anthropogenic pollution over East Asia, *Atmos. Chem. Phys.*, 2018, **18**, 7815–7825.

26 J. M. Prospero, Long-range transport of mineral dust in the global atmosphere: Impact of African dust on the environment of the southeastern United States, *Proc. Natl. Acad. Sci. U. S. A.*, 1999, **96**, 3396–3403.

27 S. Eriksen Hammer, S. Mertes, J. Schneider, M. Ebert, K. Kandler and S. Weinbruch, Composition of ice particle residuals in mixed-phase clouds at Jungfraujoch (Switzerland): enrichment and depletion of particle groups relative to total aerosol, *Atmos. Chem. Phys.*, 2018, **18**, 13987–14003.

28 A. Worringen, K. Kandler, N. Benker, T. Dirsch, S. Mertes, L. Schenk, U. Kästner, F. Frank, B. Nillius, U. Bundke, D. Rose, J. Curtius, P. Kupiszewski, E. Weingartner, P. Vochezer, J. Schneider, S. Schmidt, S. Weinbruch and M. Ebert, Single-particle characterization of ice-nucleating particles and ice particle residuals sampled by three different techniques, *Atmos. Chem. Phys.*, 2015, **15**, 4161–4178.

29 J. Lu, L. Ma, C. Cheng, C. Pei, C. K. Chan, X. Bi, Y. Qin, H. Tan, J. Zhou, M. Chen, L. Li, B. Huang, M. Li and Z. Zhou, Real time analysis of lead-containing atmospheric particles in Guangzhou during wintertime using single particle aerosol mass spectrometry, *Ecotoxicol. Environ. Saf.*, 2019, **168**, 53–63.

30 Y. Ji, X. Chen, Y. Li, W. Zhang, Q. Shi, J. Chen, Y. Gao, G. Li, J. Wang, P. Tian and T. An, The mixing state of mineral dusts with typical anthropogenic pollutants: A mechanism study, *Atmos. Environ.*, 2019, **209**, 192–200.

31 J. Guo, M. Lou, Y. Miao, Y. Wang, Z. Zeng, H. Liu, J. He, H. Xu, F. Wang, M. Min and P. Zhai, Trans-Pacific transport of dust aerosols from East Asia: Insights gained from multiple observations and modeling, *Environ. Pollut.*, 2017, **230**, 1030–1039.

32 B. G. Koffman, P. Saylor, R. Zhong, L. Sethares, M. F. Yoder, L. Hanschka, T. Methven, Y. Cai, L. Bolge, J. Longman, S. L. Goldstein and E. C. Osterberg, Provenance of Anthropogenic Pb and Atmospheric Dust to Northwestern North America, *Environ. Sci. Technol.*, 2022, **56**, 13107–13118.

33 S. Hou, N. Zheng, L. Tang, X. Ji, Y. Li and X. Hua, Pollution characteristics, sources, and health risk assessment of human exposure to Cu, Zn, Cd and Pb pollution in urban street dust across China between 2009 and 2018, *Environ. Int.*, 2019, **128**, 430–437.

34 S. Chowdhury, M. A. J. Mazumder, O. Al-Attas and T. Husain, Heavy metals in drinking water: Occurrences, implications, and future needs in developing countries, *Sci. Total Environ.*, 2016, **569**, 476–488.

35 P. K. Rai, S. S. Lee, M. Zhang, Y. F. Tsang and K.-H. Kim, Heavy metals in food crops: Health risks, fate, mechanisms, and management, *Environ. Int.*, 2019, **125**, 365–385.

36 X. Peng, G. Shi, G. Liu, J. Xu, Y. Tian, Y. Zhang, Y. Feng and A. G. Russell, Source apportionment and heavy metal health

risk (HMHR) quantification from sources in a southern city in China, using an ME2-HMHR model, *Environ. Pollut.*, 2017, **221**, 335–342.

37 Y. Hu, J. Lin, S. Zhang, L. Kong, H. Fu and J. Chen, Identification of the typical metal particles among haze, fog, and clear episodes in the Beijing atmosphere, *Sci. Total Environ.*, 2015, **511**, 369–380.

38 L. Ma, M. Li, Z. Huang, L. Li, W. Gao, H. Nian, L. Zou, Z. Fu, J. Gao, F. Chai and Z. Zhou, Real time analysis of lead-containing atmospheric particles in Beijing during springtime by single particle aerosol mass spectrometry, *Chemosphere*, 2016, **154**, 454–462.

39 W. Li, T. Wang, S. Zhou, S. Lee, Y. Huang, Y. Gao and W. Wang, Microscopic observation of metal-containing particles from Chinese continental outflow observed from a non-industrial site, *Environ. Sci. Technol.*, 2013, **47**, 9124–9131.

40 T. Hidemori, T. Nakayama, Y. Matsumi, T. Kinugawa, A. Yabushita, M. Ohashi, T. Miyoshi, S. Irei, A. Takami, N. Kaneyasu, A. Yoshino, R. Suzuki, Y. Yumoto and S. Hatakeyama, Characteristics of atmospheric aerosols containing heavy metals measured on Fukue Island, Japan, *Atmos. Environ.*, 2014, **97**, 447–455.

41 W. Kim, S.-J. Doh and Y. Yu, Asian dust storm as conveyance media of anthropogenic pollutants, *Atmos. Environ.*, 2012, **49**, 41–50.

42 Q. Wang, X. Dong, J. S. Fu, J. Xu, C. Deng, Y. Jiang, Q. Fu, Y. Lin, K. Huang and G. Zhuang, Environmentally dependent dust chemistry of a super Asian dust storm in March 2010: observation and simulation, *Atmos. Chem. Phys.*, 2018, **18**, 3505–3521.

43 K. Huang, G. Zhuang, J. Li, Q. Wang, Y. Sun, Y. Lin and J. S. Fu, Mixing of Asian dust with pollution aerosol and the transformation of aerosol components during the dust storm over China in spring 2007, *J. Geophys. Res.: Atmos.*, 2010, **115**, D00K13.

44 K. Huang, G. Zhuang, Y. Lin, J. Li, Y. Sun, W. Zhang and J. S. Fu, Relation between optical and chemical properties of dust aerosol over Beijing, China, *J. Geophys. Res.: Atmos.*, 2010, **115**, D00K16.

45 Q. Wang, G. Zhuang, J. Li, K. Huang, R. Zhang, Y. Jiang, Y. Lin and J. S. Fu, Mixing of dust with pollution on the transport path of Asian dust — Revealed from the aerosol over Yulin, the north edge of Loess Plateau, *Sci. Total Environ.*, 2011, **409**, 573–581.

46 Y. Yan, Y. B. Sun, D. Weiss, L. J. Liang and H. Y. Chen, Polluted dust derived from long-range transport as a major end member of urban aerosols and its implication of non-point pollution in northern China, *Sci. Total Environ.*, 2015, **506-507**, 538–545.

47 S. A. Kadhum, A preliminary study of heavy metals pollution in the sandy dust storms and its human risk assessment from middle and south of Iraq, *Environ. Sci. Pollut. Res.*, 2020, **27**, 8570–8579.

48 N. MalAmiri, A. Rashki, S. R. Hosseinzadeh and D. G. Kaskaoutis, Mineralogical, geochemical, and textural characteristics of soil and airborne samples during dust storms in Khuzestan, southwest Iran, *Chemosphere*, 2022, **286**, 131879.

49 S. Zahran, M. A. Laidlaw, S. P. McElmurry, G. M. Filippelli and M. Taylor, Linking source and effect: resuspended soil lead, air lead, and children's blood lead levels in Detroit, Michigan, *Environ. Sci. Technol.*, 2013, **47**, 2839–2845.

50 C. Dong, M. P. Taylor and S. Zahran, The effect of contemporary mine emissions on children's blood lead levels, *Environ. Int.*, 2019, **122**, 91–103.

51 D. J. Cziczo, O. Stetzer, A. Worringen, M. Ebert, S. Weinbruch, M. Kamphus, S. J. Gallavardin, J. Curtius, S. Borrmann, K. D. Froyd, S. Mertes, O. Moehler and U. Lohmann, Inadvertent climate modification due to anthropogenic lead, *Nat. Geosci.*, 2009, **2**, 333–336.

52 Y. Wang, H. Hu, X. Wang, H. Liu, L. Dong, G. Luo, Y. Zhao and H. Yao, A critical review on lead migration, transformation and emission control in Chinese coal-fired power plants, *J. Environ. Sci.*, 2023, **124**, 397–413.

53 M. Schindler, M. Santosh, G. Dotto, L. F. O. Silva and M. F. Hochella, A review on Pb-bearing nanoparticles, particulate matter and colloids released from mining and smelting activities, *Gondwana Res.*, 2022, **110**, 330–346.

54 Y. Batonneau, C. Bremard, L. Gengembre, J. Laureyns, A. Le Maguer, D. Le Niaguer, E. Perdrix and S. Sobanska, Speciation of PM10 sources of airborne nonferrous metals within the 3-km zone of lead/zinc smelters, *Environ. Sci. Technol.*, 2004, **38**, 5281–5289.

55 G. Uzu, S. Sobanska, Y. Aliouane, P. Pradere and C. Dumat, Study of lead phytoavailability for atmospheric industrial micronic and sub-micronic particles in relation with lead speciation, *Environ. Pollut.*, 2009, **157**, 1178–1185.

56 M. G. Tan, G. L. Zhang, X. L. Li, Y. X. Zhang, W. S. Yue, J. M. Chen, Y. S. Wang, A. G. Li, Y. Li, Y. M. Zhang and Z. C. Shan, Comprehensive Study of Lead Pollution in Shanghai by Multiple Techniques, *Anal. Chem.*, 2006, **78**, 8044–8050.

57 L. Peng, L. Li, Q. Lin, M. Li, G. Zhang, X. Bi, X. Wang and G. Sheng, Does atmospheric processing produce toxic Pb-containing compounds? A case study in suburban Beijing by single particle mass spectrometry, *J. Hazard. Mater.*, 2020, **382**, 121014.

58 G. Falgayrac, S. Sobanska, J. Laureyns and C. Bremard, Heterogeneous chemistry between $PbSO_4$ and calcite microparticles using Raman microimaging, *Spectrochim. Acta, Part A*, 2006, **64**, 1095–1101.

59 G. Falgayrac, S. Sobanska and C. Bremard, Particle-particle chemistry between micrometer-sized $PbSO_4$ and $CaCO_3$ particles in turbulent flow initiated by liquid water, *J. Phys. Chem. A*, 2012, **116**, 7386–7396.

60 T. Ishizaka, S. Tohno, C.-J. Ma, A. Morikawa, M. Takaoka, F. Nishiyama and K. Yamamoto, Reactivity between $PbSO_4$ and $CaCO_3$ particles relevant to the modification of mineral particles and chemical forms of Pb in particles sampled at two remote sites during an Asian dust event, *Atmos. Environ.*, 2009, **43**, 2550–2560.

61 R. Wischert, P. Laurent, C. Coperet, F. Delbecq and P. Sautet, gamma-Alumina: The Essential and Unexpected Role of Water for the Structure, Stability, and Reactivity of "Defect" Sites, *J. Am. Chem. Soc.*, 2012, **134**, 14430–14449.

62 M. Digne, P. Sautet, P. Raybaud, P. Euzen and H. Toulhoat, Hydroxyl groups on gamma-alumina surfaces: A DFT study, *J. Catal.*, 2002, **211**, 1–5.

63 M. Digne, P. Sautet, P. Raybaud, P. Euzen and H. Toulhoat, Use of DFT to achieve a rational understanding of acid-basic properties of gamma-alumina surfaces, *J. Catal.*, 2004, **226**, 54–68.

64 B. F. N. Wakou, M. C. Valero and P. Raybaud, Theoretical Insights into the Interaction of Oxygenated Organic Molecules and Cobalt(II) Precursor with gamma-Al_2O_3 Surfaces, *J. Phys. Chem. C*, 2018, **122**, 19560–19574.

65 A. S. Goudie and N. J. Middleton, Saharan dust storms: nature and consequences, *Earth-Sci. Rev.*, 2001, **56**, 179–204.

66 A. P. Thompson, H. M. Aktulga, R. Berger, D. S. Bolintineanu, W. M. Brown, P. S. Crozier, P. J. In't Veld, A. Kohlmeyer, S. G. Moore, T. D. Nguyen, R. Shan, M. J. Stevens, J. Tranchida, C. Trott and S. J. Plimpton, LAMMPS - a flexible simulation tool for particle-based materials modeling at the atomic, meso, and continuum scales, *Comput. Phys. Commun.*, 2022, **271**, 108171.

67 R. T. Cygan, J. J. Liang and A. G. Kalinichev, Molecular models of hydroxide, oxyhydroxide, and clay phases and the development of a general force field, *J. Phys. Chem. B*, 2004, **108**, 1255–1266.

68 S. Wang, K. Hou and H. Heinz, Accurate and Compatible Force Fields for Molecular Oxygen, Nitrogen, and Hydrogen to Simulate Gases, Electrolytes, and Heterogeneous Interfaces, *J. Chem. Theory Comput.*, 2021, **17**, 5198–5213.

69 L. Tian, *Sobtop, dev 3.1.*, http://sobereva.com/soft/Sobtop, 2023.

70 A. E. A. Allen, M. C. Payne and D. J. Cole, Harmonic Force Constants for Molecular Mechanics Force Fields via Hessian Matrix Projection, *J. Chem. Theory Comput.*, 2018, **14**, 274–281.

71 T. A. Manz and D. S. Sholl, Improved Atoms-in-Molecule Charge Partitioning Functional for Simultaneously Reproducing the Electrostatic Potential and Chemical States in Periodic and Nonperiodic Materials, *J. Chem. Theory Comput.*, 2012, **8**, 2844–2867.

72 T. A. Manz and D. S. Sholl, Chemically Meaningful Atomic Charges That Reproduce the Electrostatic Potential in Periodic and Nonperiodic Materials, *J. Chem. Theory Comput.*, 2010, **6**, 2455–2468.

73 S. Plimpton, R. Pollock and M. J. Stevens, Particle Mesh Ewald and RRESPA for Parallel Molecular Dynamics Simulations., in *Proceedings of Eighth SIAM Conference on Parallel Processing for Scientific Computing*, 1997, pp. 1–13.

74 A. Stukowski, Visualization and analysis of atomistic simulation data with OVITO–the Open Visualization Tool, *Modell. Simul. Mater. Sci. Eng.*, 2010, **18**, 015012.

75 W. Humphrey, A. Dalke and K. Schulten, VMD: visual molecular dynamics, *J. Mol. Graphics*, 1996, **14**(33–38), 27–38.

76 T. Giorgino, Computing 1-D atomic densities in macromolecular simulations: The density profile tool for VMD, *Comput. Phys. Commun.*, 2014, **185**, 317–322.

77 G. Kresse and J. Furthmüller, Efficient iterative schemes for ab initio total-energy calculations using a plane-wave basis set, *Phys. Rev. B: Condens. Matter Mater. Phys.*, 1996, **54**, 11169–11186.

78 J. P. Perdew, J. A. Chevary, S. H. Vosko, K. A. Jackson, M. R. Pederson, D. J. Singh and C. Fiolhais, Atoms, molecules, solids, and surfaces: Applications of the generalized gradient approximation for exchange and correlation, *Phys. Rev. B: Condens. Matter*, 1993, **46**, 6671–6687.

79 P. E. Blöchl, Projector augmented-wave method, *Phys. Rev. B: Condens. Matter*, 1994, **50**, 17953–17979.

80 S. Grimme, S. Ehrlich and L. Goerigk, Effect of the Damping Function in Dispersion Corrected Density Functional Theory, *J. Comput. Chem.*, 2011, **32**, 1456–1465.

81 S. Grimme, J. Antony, S. Ehrlich and H. Krieg, A consistent and accurate ab initio parametrization of density functional dispersion correction (DFT-D) for the 94 elements H-Pu, *J. Chem. Phys.*, 2010, **132**, 154104.

82 R. Nelson, C. Ertural, J. George, V. L. Deringer, G. Hautier and R. Dronskowski, LOBSTER: Local orbital projections, atomic charges, and chemical-bonding analysis fromprojector-augmented-wave-baseddensity-functional theory, *J. Comput. Chem.*, 2020, **41**, 1931–1940.

83 R. Dronskowski and P. E. Bloechl, Crystal orbital Hamilton populations (COHP): energy-resolved visualization of chemical bonding in solids based on density-functional calculations, *J. Phys. Chem.*, 1993, **97**, 8617–8624.

84 J. Heyd, G. E. Scuseria and M. Ernzerhof, Hybrid functionals based on a screened Coulomb potential, *J. Chem. Phys.*, 2003, **118**, 8207–8215.

85 W. Nie, A. Ding, T. Wang, V. M. Kerminen, C. George, L. Xue, W. Wang, Q. Zhang, T. Petaja, X. Qi, X. Gao, X. Wang, X. Yang, C. Fu and M. Kulmala, Polluted dust promotes new particle formation and growth, *Sci. Rep.*, 2014, **4**, 6634.

86 P. Liang, B. Chen, X. Yang, Q. Liu, A. Li, L. Mackenzie and D. Zhang, Revealing the dust transport processes of the 2021 mega dust storm event in northern China, *Sci. Bull.*, 2022, **67**, 21–24.

87 S. Li, J. Wu, Y. Huo, X. Zhao and L. Xue, Profiling multiple heavy metal contamination and bacterial communities surrounding an iron tailing pond in Northwest China, *Sci. Total Environ.*, 2021, **752**, 141827.

88 H. Luo, Q. Wang, Q. Guan, Y. Ma, F. Ni, E. Yang and J. Zhang, Heavy metal pollution levels, source apportionment and risk assessment in dust storms in key cities in Northwest China, *J. Hazard. Mater.*, 2022, **422**, 126878.